Quantum phase transition and ferromagnetism in $Co_{1+x}Sn$

Rabindra Pahari,[1,2] Balamurugan Balasubramanian,[1,2,*] Rohit Pathak,[3] Manh Cuong Nguyen,[4,5] Shah R. Valloppilly,[1] Ralph Skomski,[1,2] Arti Kashyap,[3] Cai-Zhuang Wang,[4,5] Kai-Ming Ho,[4,5] George C. Hadjipanayis,[6] and David J. Sellmyer[1,2,†]

[1]*Nebraska Center for Materials and Nanoscience, University of Nebraska, Lincoln, Nebraska 68588, USA*

[2]*Department of Physics and Astronomy, University of Nebraska, Lincoln, Nebraska 68588, USA*

[3]*School of Basic Sciences, IIT Mandi, Mandi, Himachal Pradesh 175005, India*

[4]*Ames Laboratory, US Department of Energy, Ames, Iowa 50011, USA*

[5]*Department of Physics and Astronomy, Iowa State University, Ames, Iowa 50011, USA*

[6]*Department of Physics and Astronomy, University of Delaware, Newark, Delaware 19716, USA*

(Received 22 April 2019; revised manuscript received 9 May 2019; published 28 May 2019)

The onset of ferromagnetism in cobalt-tin alloys is investigated experimentally and theoretically. The $Co_{1+x}Sn$ alloys were prepared by rapid quenching from the melt and form a modified hexagonal NiAs-type crystal structure for $0.45 \leqslant x \leqslant 1$. The magnetic behavior is described analytically and by density-functional theory using supercells and the coherent-potential approximation. The excess of Co concentration x, which enters the interstitial $2d$ sites in the hypothetical NiAs-ordered parent alloy CoSn, yields a Griffiths-like phase and, above a quantum critical point ($x_c \approx 0.65$), a quantum phase transition to ferromagnetic order. Quantum critical exponents are determined on the paramagnetic and ferromagnetic sides of the transition and related to the nature of the magnetism in itinerant systems with different types of chemical disorder.

DOI: 10.1103/PhysRevB.99.184438

I. INTRODUCTION

Quantum phase transitions (QPTs), defined as continuous phase transitions at zero temperature, have remained an intriguing research topic [1–6]. There are several types of QPTs, dealing with various classes of materials, such as magnets [7–9], superconductors [10], heavy-fermion compounds [11,12], and ferroelectrics [13], and triggered by different control parameters, for example mechanical pressure, magnetic or electric fields, and chemical composition [14–16]. In some solid-solution alloys of type $M_{1-x}T_x$ [2,17,18] magnetic transition-metal elements (T) cause the nonmagnetic metal (M) to become a ferromagnet above some critical concentration x_c. The chemical disorder in QPT alloys is normally of the substitutional solid-solution type, with nearest-neighbor exchange bonds. This paper deals with QPTs caused by interstitial modification of an intermetallic compound.

We consider alloys having the composition $Co_{1+x}Sn$ ($0 < x \leqslant 1$), where the excess Co (x) enters the $2d$ interstitial sites in the NiAs structure (Fig. 1) [19,20]. Current research on Co-based alloys is partly motivated by the need to discover new magnetic materials with high Curie temperature, high anisotropy, and high magnetization. Such materials, especially consisting of earth-abundant and inexpensive elements, are needed for advanced energy and information-processing applications [21–23]. New Co- and/or Fe-rich compounds, especially those with noncubic and/or metastable structures, are of particular interest, since they potentially possess the above desirable magnetic properties. The $Co_{1+x}Sn$ system is compelling because the local-environment effects and associated spin-cluster effects are nontrivial, and whether the apparent quantum phase transition is similar to or distinguishable from other examples is intriguing [5].

Thermodynamic phase transitions such as Curie transitions and QPTs have many features in common but also exhibit important differences. A common feature is that both types of transitions are typically described by power laws that relate the response of the system to control parameters. Our focus is on magnetic alloys, where the order parameter (magnetization M) and the susceptibility χ are controlled by the temperature T, the magnetic field H, and the chemical composition x. For example, structurally homogeneous ferromagnets near the Curie temperature T_c obey $M \sim (T_c - T)^{\beta}$ and $\chi \sim 1/|T_c - T|^{\gamma}$ [24]. The susceptibility diverges near the critical point, and this divergence is accompanied by long-range critical fluctuations. These fluctuations, observed for example as critical opalescence in fluids, have correlation length $\xi \sim 1/|T_c - T|^{\nu}$ [24,25]. A major difference is that QPTs reflect quantum-mechanical fluctuations, as contrasted to the thermodynamic fluctuations governing the critical behavior of ferromagnets (Curie transition) and of fluids (gas-liquid transition).

The description of critical behavior and the determination of critical exponents are nontrivial, especially in low-dimensional systems [24–27]. For example, it is well known that long-range fluctuations yield $T_c = 0$ in one-dimensional magnets [25,26,28]. The simplest approach towards critical phenomena is the mean-field approximation (MFA), where the crystalline environment of a given atom is modeled as an effective medium. In this paper, we distinguish between three types of mean-field approximations, namely thermodynamic MFA (Landau theory), quantum-mechanical MFA

*bbalasubramanian2@unl.edu

†dsellmyer@unl.edu

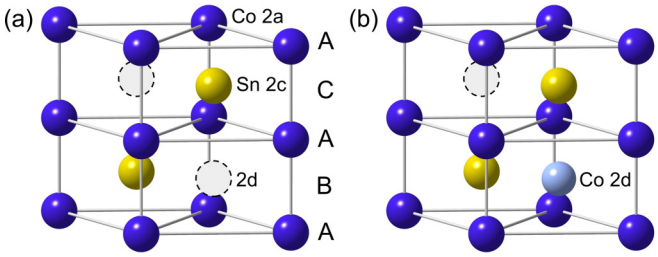

FIG. 1. Unit cell of NiAs-ordered $Co_{1+x}Sn$: (a) CoSn and (b) $Co_{1.5}Sn$. The excess Co (x) occupies the interstitial $2d$ sites, which exhibit a trigonal-prismatic coordination by the Co atoms of the CoSn host lattice.

(Stoner theory), and structural MFA (Bethe-lattice percolation theory).

In its simplest form, the mean-field theory of thermodynamic phase transitions considers the order parameter $\boldsymbol{M} = M\boldsymbol{e}_z$ and assumes a Landau free energy

$$F = \tfrac{1}{2}a_0(T - T_c)M^2 + \tfrac{1}{4}a_4M^4 - \mu_0 HM, \tag{1}$$

where a_0 and a_4 are materials constants and $M = \langle M(\boldsymbol{r})\rangle$. Putting $\partial F/\partial M = 0$ in this equation yields the familiar mean-field exponents $\beta = 1/2$ and $\gamma = 1$. An alternative way of deriving these exponents is to replace the field H acting on an atomic spin by $H + \lambda M$, where λ is referred to as molecular- or mean-field coefficient.

The assumption of an effective medium of average magnetization $\langle M\rangle$ does not necessarily mean that the local magnetization $M(\boldsymbol{r})$ of homogeneous solids is equal to the average magnetization $\langle M\rangle$. The corresponding fluctuations are described by the correlation function

$$C(|\boldsymbol{r} - \boldsymbol{r}'|) = [M(\boldsymbol{r}) - \langle M\rangle][M(\boldsymbol{r}') - \langle M\rangle]. \tag{2}$$

The zero-field correlations decay as $C(|\boldsymbol{r} - \boldsymbol{r}'|) \sim \exp(-\xi/(|\boldsymbol{r} - \boldsymbol{r}'|))$.

Completely ignoring $C(|\boldsymbol{r} - \boldsymbol{r}'|)$ corresponds to the Landau theory of Eq. (1), but the Ornstein-Zernike extension of the Landau theory includes fluctuations on a mean-field level [24,27]. The extension is obtained by adding a Ginzburg-type gradient term $(\nabla M)^2$ to Eq. (1). This term means that interatomic exchange diminishes pronounced magnetization fluctuations. The Ornstein-Zernike theory yields the wave-vector-dependent Curie-Weiss susceptibility

$$\chi(k) = \frac{\chi_0}{1 - T/T_c + wk^2}, \tag{3}$$

where the parameter w is quadratic in the lattice parameter a.

The quantum-mechanical mean-field approximation deals with electron-electron interactions and treats surrounding electrons as an effective medium (electron gas). In this case, Eq. (1) must be replaced by the conceptually very similar expression

$$E = \tfrac{1}{2}a_2M^2 + \tfrac{1}{4}a_4M^4 - \mu_0 MH. \tag{4}$$

Here $a_2 \sim 1/\mathcal{D}(E_F) - I$, where I, $\mathcal{D}(E_F)$, and H are Stoner parameter, density of states at the Fermi level, and external magnetic field, respectively. This approximation ignores electron correlations (the Coulomb interaction between individualized electrons) but is normally a good approximation for itinerant systems, such as Co-Sn. The corresponding wave-vector-dependent susceptibility is [29,30]

$$\chi(k) = \frac{\chi_0}{1 - I\mathcal{D}(E_F) + wk^2}. \tag{5}$$

This equation, where $w \approx 2I\mathcal{D}(E_F)/{k_F}^2$, describes the low-temperature susceptibility. Due to spin fluctuations, Eq. (5) is difficult to generalize to finite temperatures, but for reasons discussed elsewhere [30–32], high-temperature susceptibilities of itinerant magnets are often of the Curie-Weiss type, Eq. (3).

A third type of mean-field theory is related to the percolation aspect of disordered alloys. Randomly distributing Co atoms over the interstitial sites creates Co-rich clusters and Co-poor regions, and ferromagnetism develops from Co-rich clusters. In fact, even below the onset of long-range ferromagnetic order, some clusters are very big, which causes the susceptibility to exhibit a quasiferromagnetic singularity known as the Griffiths singularity; the corresponding region is referred to as Griffith phase [2,33–36]. With increasing x, the Co clusters grow, and at some initial percolation threshold x_c, an infinite backbone develops. Below x_c, the average cluster size has the character of a correlation length, obeying $\xi \sim 1/(x_c - x)^{\nu}$ [37,38].

The mean-field description of percolation is that of the Bethe lattice [38] and yields the mean-field exponent $\nu = 1/2$. The same mean-field exponent is obtained from Eq. (3), where $\xi \sim 1/(1 - T/T_c)^{1/2}$, and from Eq. (5), where $\xi \sim 1/[1 - I\mathcal{D}(E_F)]^{1/2}$. These correlation lengths all diverge at the critical point. One question considered in this paper is how the different correlation lengths interact with each other in the cobalt-tin system.

Our emphasis is on length scales of a few interatomic distances, partially going beyond mean-field theory. In the experimental part, Sec. II, the Co-Sn alloys are investigated using structural and magnetic measurements, whereas Sec. III is devoted to analytical and density-functional theoretical calculations, as well as an analysis of the data in terms of a quantum phase transition.

II. EXPERIMENTAL METHODS AND RESULTS

Samples of bulk $Co_{1+x}Sn$ ($0.45 \leqslant x \leqslant 1.0$) were fabricated by conventionally arc melting appropriate amounts of Co and Sn, followed by rapid quenching from the melt using a melt-spinning method. A wheel speed of 40 m/s was used to melt spin the arc-melted samples into ribbons. The additional melt-spinning step was motivated to achieve a broad high-temperature homogeneity range of alloys such as Co-Sn [20]. The composition of the alloys was measured by energy-dispersive x-ray spectroscopy, using a spectrometer attached to a secondary-electron microscope (FEI Nova NanoSEM 450). The structural properties were investigated with a Rigaku SmartLab x-ray diffractometer using $Cu\,K_\alpha$ radiation, which has a wavelength of 1.5406 Å. A Quantum Design MPMS superconducting quantum interference device and a physical property measurement system were used to measure the magnetic properties of the Co-Sn samples.

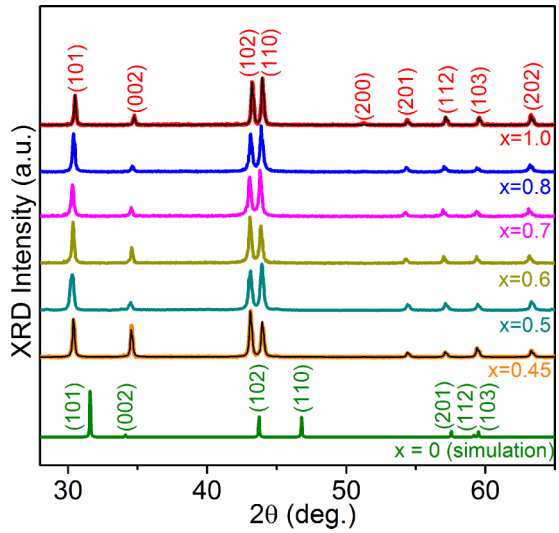

FIG. 2. X-ray-diffraction patterns of the $Co_{1+x}Sn$ samples indexed using standard x-ray-diffraction data for $Co_{1.5}Sn$ alloy with NiAs-type hexagonal structure [39]. The black curves on the experimental XRD patterns for $x = 0.45$ and 1 represent the corresponding fitted curves using Rietveld analysis based on interstitial occupation of excess Co. A simulated x-ray-diffraction pattern for CoSn ($x = 0$) with the hypothetical NiAs-type structure is also shown for comparison.

A. Structure

The parent structure of $Co_{1+x}Sn$ alloys is the hexagonal $B8_1$ structure (prototype NiAs, space group $P6_3/mmc$). As shown in Fig. 1(a), the NiAs structure has the layer stacking *ABAC*, as compared to the *AB* and *ABC* stackings of the hcp and fcc structures. The Sn atoms (yellow) occupy the 2*c* sites in the *B* and *C* layers. In a hypothetical equiatomic NiAs-ordered CoSn [Fig. 1(a)], the Co atoms (dark blue) occupy the 2*a* sites in the *A* planes only, leaving the interstitial 2*d* sites empty. The extra Co atoms (light blue) occupy a fraction *x* of the interstitial sites in the *B* and *C* planes, in Fig. 1(b).

NiAs-type $Co_{1+x}Sn$ exists over a broad composition range [19,20]. However, the NiAs structure is unstable for equiatomic CoSn, which crystallizes in the unrelated hexagonal *B*35 structure (prototype CoSn, space group $P6/mmm$). Some excess Co ($x > 0$) is therefore necessary to stabilize the NiAs structure. The idealized case of complete interstitial occupancy ($x = 1$) corresponds to the $B8_2$ structure (prototype Ni_2In, $P6_3/mmc$), which is a modified NiAs structure.

The experimental x-ray-diffraction (XRD) patterns for the melt-spun $Co_{1+x}Sn$ ($0.45 \leqslant x \leqslant 1$) alloys are shown in Fig. 2 and analyzed by Rietveld refinement using models based on both site mixing of Co and Sn as well as interstitial occupation of excess Co. From the simulations of powder XRD, relative intensity variation of (101), (102), and (110) diffraction peaks provides important evidence on the site occupancy of Co. If the Co atoms were to replace Sn at the 2*c* site, the diffraction peak (101) always remains the most intense peak. In contrast, an increasing occupation of excess Co at the interstitial 2*d* site leads to a gradual increase of the relative intensities of (102) and (110) in comparison to (101) peak. We have observed the latter behavior in our experimental XRD patterns, which strongly suggests the interstitial occupation of the excess Co. Co-Sn site mixing up to 10% cannot be ruled out, but the predominant mechanism can be established as the interstitial occupation of excess Co as evident from the fitting results. For example, the fitted XRD curves for $x = 0.45$ and $x = 1$ based on interstitial occupation of excess Co are shown in Fig. 2 and exhibit good agreement with the experimental XRD patterns. We also have simulated XRD pattern for the equiatomic CoSn with the hypothetical NiAs-type structure using density-functional theory (DFT)-optimized lattice parameters (Sec. III B) and included in Fig. 2 for a comparison. There are two most significant differences between the XRD patterns on the interstitially modified alloys ($0.45 \leqslant x \leqslant 1$) and that of the equiatomic CoSn compound; (i) the (101) reflection is the most intense for $x = 0$, whereas the (102) and (110) reflection shows most intense peaks for $0.45 \leqslant x \leqslant 1$; (ii) the position of the XRD peaks for $x = 0$ exhibit significant shifts as compared to those for interstitially modified alloys due to the difference in lattice parameters.

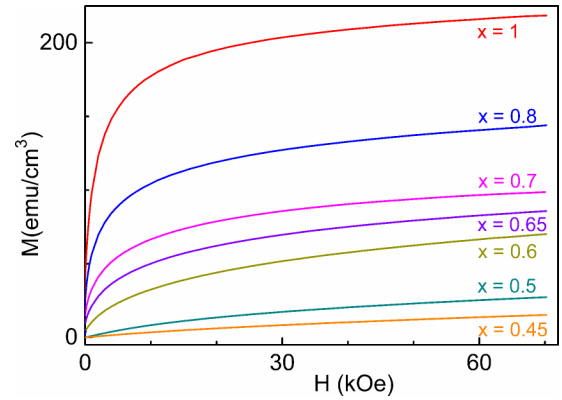

FIG. 3. Magnetic-field dependence of the magnetization of $Co_{1+x}Sn$ alloys measured at 10 K.

B. Magnetism

Figure 3 shows the magnetization at 10 K as a function of the external magnetic field for $0.45 \leqslant x \leqslant 1$ in $Co_{1+x}Sn$ and reveals an apparent transition from paramagnetism to ferromagnetism between $x = 0.45$ and $x = 1$. In brief, the samples having $x = 0.45 - 0.65$ are far away from saturation, typical paramagnetic behavior. The Co-rich samples exhibit a ferromagnetic signature, with near saturation in relatively low fields; i.e., the results indicate that cobalt addition stimulates the onset of ferromagnetism in the range $0.6 \leqslant x \leqslant 0.7$. For example, the temperature dependence of $M(H)$ indicates paramagnetism for $x = 0.5$ and ferromagnetism for $x = 0.8$ as shown in Figs. 4(a) and 4(b), respectively.

The temperature dependence of the magnetization in a field of 1 kOe, inset of Fig. 4(b), also shows that the $x = 0.7$ and $x = 0.8$ samples are ferromagnetic with Curie temperatures of about 650 and 660 K, respectively. The $M(T)$ behavior of the alloy with $x = 1$ suggests a Curie temperature well above 900 K. An upturn was observed at 700 K for $x = 0.7$ and 840 K for $x = 0.8$, not shown in the inset of Fig. 4(b), which is possibly due to the decomposition of the Co-Sn alloys into Co and Sn. Our measurements indicate a magnetic phase

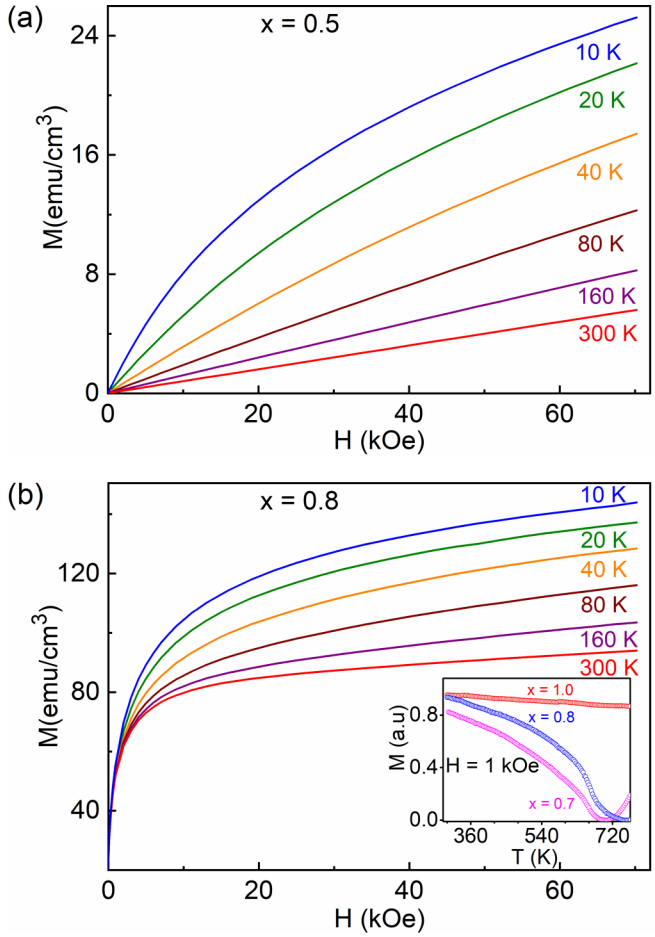

FIG. 4. Field-dependent magnetization measured at different temperatures: (a) $x = 0.5$ and (b) $x = 0.8$. The inset in (b) shows the $M(T)$ curves in an external field of 1 kOe for $x = 0.7, 0.8$, and 1.0.

transition to ferromagnetic long-range order immediately above $x = 0.65$.

The high-field magnetization at 10 K was analyzed for the ferromagnetic samples by the standard law of approach to saturation: $M(H) = M_s[1 - A/H^2]$, where M_s is the saturation magnetization, and A is related to the intrinsic magnetic anisotropy [40]. The M_s values for the $x = 0.7, 0.8$, and 1.0 samples are shown in Table I and these lead to estimates of the average moments per formula unit (f.u.), also shown in Table I.

As shown in Fig. 5(a), the $Co_{1+x}Sn$ samples having $x = 0.45 - 0.65$ are paramagnetic with low-temperature upturns in the susceptibility. We interpret this as a Griffiths phase

TABLE I. Properties of the ferromagnetic $Co_{1+x}Sn$ samples at 10 K.

x	M_s (emu/cm^3)	M_s (μ_B/f.u.)
0.7	77	0.32
0.8	128	0.53
1.0	195	0.80

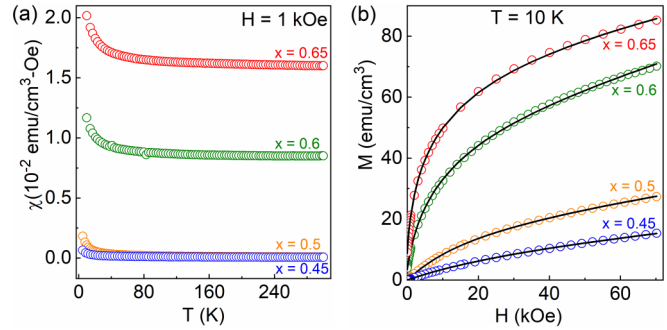

FIG. 5. (a) Temperature-dependent susceptibility and (b) field-dependent magnetization measured at 10 K fitted to a Langevin function. The open circles correspond to the experimental data and solid lines represent fitting results.

effect involving cluster moments embedded in a Pauli paramagnetic host matrix. Analysis of the low-temperature data in terms of a simple Curie or Curie-Weiss expression is not possible in this case because the cluster density as a function of x is unknown. For this reason, in Fig. 5(b) we have fitted the experimental magnetization for the samples with $x = 0.45 - 0.65$ to the Langevin expression,

$$M = \chi_0 H + M_s^{\text{cluster}} \mathcal{L}\left[\frac{1}{k_B T}\left(\mu_0 m H + \mathcal{J}\frac{M}{M_s^{\text{cluster}}}\right)\right], \quad (6)$$

where m and M_s^{cluster} are the magnetic moment and saturation magnetization of the clusters, respectively, and χ_0 is the Pauli susceptibility. The measured data and the fitted curves are in good agreement. The fitting parameters M_s^{cluster}, m, and $\mathcal{J}$ will be discussed in Sec. III A.

III. DISCUSSION

While NiAs-ordered CoSn does not exist as an equilibrium phase [19,20], small amounts x of interstitial Co stabilize the phase. With increasing x, the phase is initially nonmagnetic, but then local moments appear, magnetic clusters form, and a Griffiths phase develops. Above a critical value x_c, the system develops long-range ferromagnetic order. In cluster systems, the onset of long-range ferromagnetism is a percolation effect, roughly corresponding to the geometrical percolation of the interstitial-cobalt regions. In this section, we analyze theoretical aspects of these transitions, both analytically and numerically. The exact numerical treatment of structural and magnetic percolation effects is nontrivial and requires complicated methods such as renormalization-group theory [25] and Monte Carlo simulations [38], which go beyond the scope of this paper. However, much nontrivial physics emerges from the analysis of some specific aspects of the interstitially modified alloy. We first focus on cluster moment formation in the paramagnetic phase. Then we use spin-polarized electronic-structure calculations to describe the onset of ferromagnetism. Finally, we determine the extent to which our results can be understood in terms of recent ideas on quantum phase transitions.

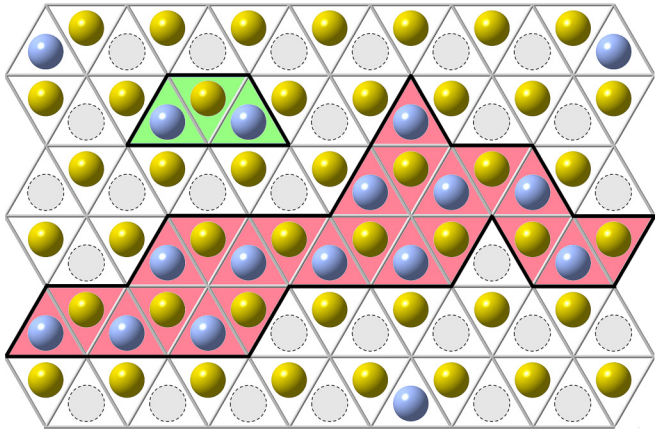

FIG. 6. Percolation and Griffith phase in the B and C planes of the modified NiAs structure. Isolated interstitial Co atoms (blue) are nonmagnetic, but small clusters of interstitial atoms (light green) develop a local magnetic moment. Sufficiently high interstitial Co contents yield a percolating backbone (light red), which corresponds to the onset of ferromagnetism [38]. The percolation criterion used in this figure (site percolation involving Sn atoms) is only approximate, due to interatomic wave-function overlap.

A. Cluster moments and percolation

Figure 6 illustrates the moment formation and percolation aspects of the interstitial $Co_{1+x}Sn$ by considering the B and C layers, which are equivalent aside from a shift $\frac{1}{2}(\boldsymbol{a}+\boldsymbol{b})$ in the a-b plane. Small interstitial concentrations x correspond to isolated Co atoms in the B and C planes, but with increasing x, clusters rich in interstitial Co start to form (light green). The number and sizes of the clusters increase with x, and at some percolation threshold x_p, an infinite backbone cluster emerges (light red). The geometrical percolation transition at x_p roughly corresponds to the onset of long-range ferromagnetic order (x_c). In fact, there are several types of percolation even in a geometrical sense, such as site- and bond percolation [38]. Figure 6 corresponds to a special type of site percolation, where two interstitial Co atoms are connected if they share sides with a common Sn atom. If two Co atoms are connected by this rule, they also share two trigonal-prismatically coordinating A-layer atoms, which is favorable for the development of interatomic exchange across layers. By comparison, the bond-percolation equivalent of this rule, which connects two interstitial Co atoms in a B or C layer if they share *corners* with a common Sn atom, does not lead to this type of interlayer coupling.

Below percolation, there exists a broad range of non-or weakly interacting clusters, including a small fraction of big but finite clusters that correspond to the Griffiths phase [2,33–36]. Even above x_p, some of the clusters remain unconnected and therefore paramagnetic (light green in Fig. 6). The question arises whether unconnected clusters have a magnetic moment. The existence of local magnetic moments in disordered metallic structures is a well-studied problem. The physics underlying this phenomenon often is discussed in terms of the Anderson model, where atomic d levels are polarized and split by the d-d interaction and then broadened into resonances by hybridization with s electrons [41]. Since the present system is metallic and without strong correlations, it is reasonable to consider the use of DFT based on the local spin-density approximation. The actual moment formation cannot be predicted in a simple way from the site- or bond-percolation thresholds, and explicit electronic-structure calculations are necessary to predict the moments (Sec. III B).

TABLE II. Properties of clusters in $Co_{1+x}Sn$ obtained using Langevin fitting of $M(H)$ curves.

x	M_s^{cluster} (emu/cm^3)	m (μ_B)	$\mathcal{J}/k_B$ (K)	ρ (nm^{-3})	D (nm)
0.45	8.1	0.98	18.5	0.90	1.29
0.5	24.3	2.8	21.5	0.94	1.27
0.6	60.4	5.41	26.6	1.20	1.17
0.65	88.1	6.87	28.5	1.38	1.11

Figure 5(b) makes it possible to determine the average cluster moment m as a function of x, and an effective cluster density ρ, which can be defined through $M_s^{\text{cluster}} = \rho m$. The values of M_s^{cluster}, m, and $\mathcal{J}$ obtained from Langevin fitting are given in Table II.

Figure 7 shows plots of m and $\mathcal{J}/k_B$ as functions of x. Both the cluster moment m and the intercluster exchange $\mathcal{J}$ increase with x, and the positive sign of $\mathcal{J}$ is consistent with ferromagnetic coupling between the clusters.

The values $\rho = M_s^{\text{cluster}}/m$ of cluster density are shown in Table II and range from 0.90 to 1.38 (nm)$^{-3}$ on varying x from 0.45 to 0.65. The clusters are randomly distributed, but the center-to-center distance D between neighboring clusters is approximately twice the Wigner-Seitz cell radius of the corresponding three-dimensional Voronoi mosaic, $D = (6/\pi\rho)^{1/3}$. This distance decreases from 1.29 to 1.11 nm on increasing x from 0.45 to 0.65 (Table II).

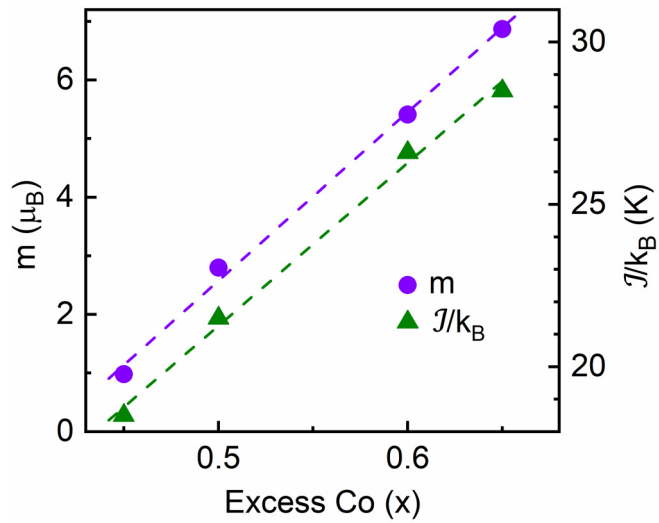

FIG. 7. Dependence of cluster moment (m) and intercluster exchange ($\mathcal{J}/k_B$) on x (excess Co). The lines are simply guides to the eye.

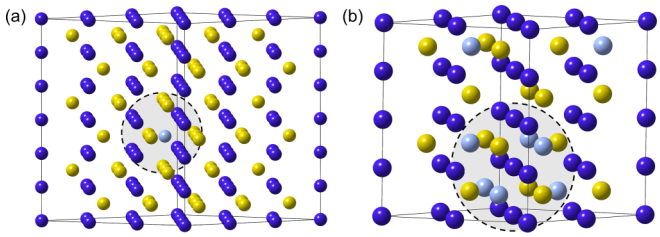

FIG. 8. Moment formation in interstitial $Co_{1+x}Sn$: (a) single interstitial Co atom in a $3 \times 3 \times 3$ supercell, corresponding to a net composition $Co_{1.02}Sn$ and (b) magnetic cluster (light gray) in a $2 \times 2 \times 2$ supercell, corresponding to $Co_{1.5}Sn$.

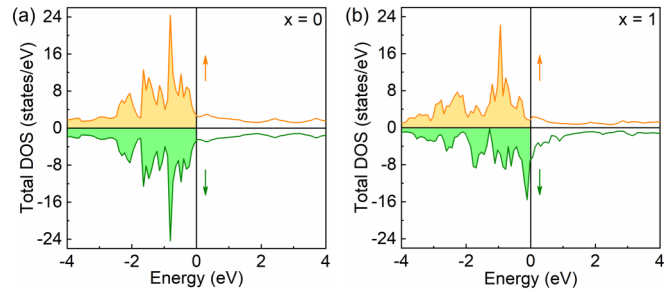

FIG. 9. Total density of states from DFT calculations: (a) CoSn (paramagnetic) and (b) Co_2Sn (ferromagnetic). The ferromagnetism can be seen from the spin-dependent shift of the dominant Co $3d$ peak just below the Fermi level.

B. Electronic-structure calculations

To calculate the magnetic moments of individual atoms, we have used density-functional theory as implemented in the Vienna *Ab initio* Simulation Package (VASP) [42]. The method involves an accurate frozen-core projector-augmented plane-wave (PAW) method. We employ PAW pseudopotentials, with exchange and correlation described by Perdew, Burke, and Ernzerhof (PBE), using a generalized-gradient approximation (GGA) [43]. A kinetic-energy cutoff of 500 eV was taken for the plane-wave basis set and the equilibrium lattice parameters were obtained by relaxing the unit cell using the conjugate-gradient method with a highly accurate convergence limit of 10^{-6} eV. We used different sizes of the k-point grid for different unit cells for the calculations in the irreducible part of the Brillouin zone, employing the Monkhorst-Pack scheme [44].

To model the atomic structure of the interstitial alloys, we have constructed several supercells slightly above $x = 0$, using DFT-optimized lattice parameters of $a = 3.88$ Å and $c = 5.25$ Å for the hypothetical CoSn alloy ($x = 0$). For $x \geqslant 0.38$, the relaxed lattice parameters obtained using calculations are similar to the experimental lattice parameters. A random-number generator was used to assign occupancies of 0 (empty) or 1 (Co) to the individual $2d$ sites. To avoid off-stoichiometric (Co-poor or Co-rich) supercells, configurations having too few or too many Co atoms were discarded. The largest supercell considered is that of Fig. 8(a), a $3 \times 3 \times 3$ supercell containing between 108 and 162 atoms and corresponding to the $Co_{1.02}Sn$ stoichiometry.

Our calculations predict that hypothetical CoSn is nonferromagnetic. The same is true for a single interstitial Co atom in a large supercell [Fig. 8(a)], which is unable to create a local magnetic moment, in spite of its trigonal-prismatic coordination by six Co atoms on the $2a$ sites. Note that the Wigner-Seitz cell radius established by the interstitial Co sublattice of Fig. 8(a) is 0.79 nm. This figure can therefore be used to gauge the center-to-center cluster distance of Sec. III A.

Adding further Co atoms to the structure of Fig. 8(a) has two effects. A part of the additional Co atoms occupies interstitial sites in Co-poor regions and remains nonmagnetic. However, some added Co atoms are close to interstices already occupied, forming or enlarging Co-rich magnetic clusters (gray circle). The formation of clusters enhances the cluster density ρ, but some added Co atoms provide percolation bridges between existing clusters and thereby reduce ρ. This means that additional Co primarily increases the cluster size, as opposed to the number of clusters.

We have found that relatively small clusters of interstitial Co atoms develop a magnetic moment, largely but not exclusively confined to the central (interstitial) atoms and the coordinating Co prism. The situation is schematically depicted in Fig. 8(b), where the atoms in the gray circle are spin polarized. The atomic moments strongly depend on more distant interstitial Co atoms, and we have not attempted to systematically analyze the configurational aspect of the problem. A very transparent picture is obtained for $x = 1$, where the atomic moments per atom are $0.99\,\mu_B$(Co $2a$), $0.33\,\mu_B$(Co $2d$), and $-0.06\,\mu_B$(Sn $2c$).

For comparison, the calculated total densities of states for $x = 0$ and $x = 1$ are shown in Fig. 9(a) and Fig. 9(b), respectively. The $\uparrow$ and $\downarrow$ bands are identical for $x = 0$ (paramagnetism). For $x = 1$, the $\uparrow$ and $\downarrow$ bands are different, the alloys are ferromagnetic, and the calculations yield an average magnetic moment of $0.66\,\mu_B$/Co for $x = 1$, in a rough agreement with the experimental value, $0.8\,\mu_B$/f.u. or $0.40\mu_B$/Co (Table I).

We also have performed first-principle spin-polarized DFT calculations within the coherent-potential approximation (CPA) [45]. The GGA, parametrized by PBE [43], was employed along with the spin-polarized relativistic Korringa-Kohn-Rostoker (SPR-KKR) code from the Munich group [46,47]. The calculations were carried out in scalar-relativistic mode with a dense $32 \times 32 \times 32$ k-point mesh. The experimental lattice parameters were used in the calculations. The $2a$ site is always fully occupied by Co. Sn occupies the $2c$ site. The interstitial $2d$ site is partially or fully occupied by Co depending on the value of x.

In the CPA [45,48], individual interstitial sites (Co filled or empty) are treated accurately, but the surrounding atoms are modeled as an effective medium. This single-site approximation is a major advantage and fairly accurately describes most physical properties. However, one of its shortcomings is the neglect of cluster localization. For example, band edges calculated using the CPA are unphysically sharp [49,50]. In the present context, cluster localization means that the magnetism of the Co atom depends on whether it is located in a Co-rich cluster or in a Co-poor region. In the former case, it becomes spin polarized easily, and this effect is ignored by the CPA. As a consequence, the CPA largely ignores Griffiths

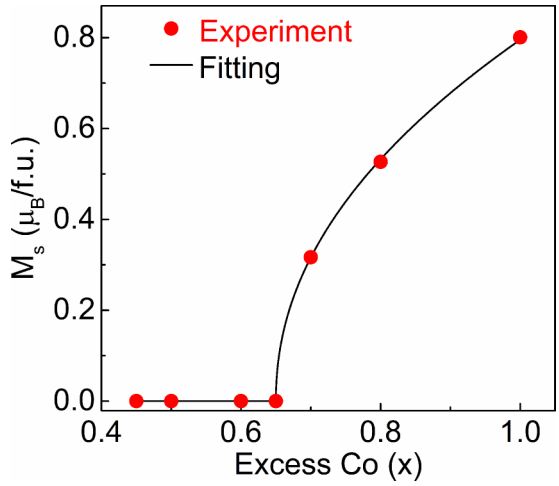

FIG. 10. Measured saturation magnetization at 10 K for the $Co_{1+x}Sn$ as a function of x (solid circles). The curved line corresponds to the fitting of the experimental data using $M_s \sim (x - x_c)^{\beta'}$.

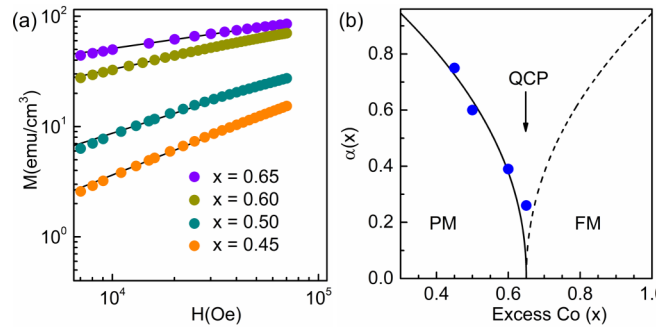

FIG. 11. Power-law analysis of the field dependence of the magnetization: (a) experimental $M(H)$ curves measured at 10 K for $Co_{1+x}Sn$ (solid circles). The solid lines correspond to the fitting using $M \sim H^{\alpha}$; (b) the nonuniversal exponent $\alpha(x)$, solid circles, fitted by $\alpha(x) \sim (x_c - x)^{\zeta}$ (solid line). The dashed line is drawn exactly symmetric to the solid line to explain the quantum critical behavior.

phase effects and underestimates the formation of magnetic moments for low Co contents. In brief, the CPA calculations agree with the experimental magnetic behaviors observed for $x = 0.5$ and $x = 1$ in $Co_{1+x}Sn$ alloys, meaning that $Co_{1.5}Sn$ is paramagnetic and Co_2Sn is ferromagnetic with $0.26\,\mu_B$ per Co, which agrees qualitatively with the corresponding experimental value ($0.40\,\mu_B$/Co) (Table I).

C. Quantum phase transition analysis

The onset of ferromagnetic order in the present system is generated by the quantum fluctuations induced by the excess Co in $Co_{1+x}Sn$, that is, it is determined ultimately by the density of states (DOS) at the Fermi level, as discussed in Sec. I. For example, the DOS can be tuned by changing the chemical composition of an alloy $M_{1-x}T_x$ with ferromagnetism occurring above x_c, the quantum critical point, and the saturation magnetization eventually follows the power law $M_s \sim (x - x_c)^{\beta'}$, where β' is a critical exponent [51]. We have fitted the experimental M_s values of the ferromagnetic $Co_{1+x}Sn$ samples (Table I) using this power law [Fig. 10], and this analysis yields $\beta' = 0.47 \pm 0.03$ and $x_c = 0.65 \pm 0.01$, that is, the magnetic QPT to ferromagnetism in the $Co_{1+x}Sn$ alloys occurs at x_c of about 0.65. Our analysis shows a comparatively strong dependence of β' on the variation of x_c within the error bar.

We also consider QPT in $Co_{1+x}Sn$ alloys following another approach used by Wang *et al.* in $Ni_{1-x}V_x$ [2]. This study shows that the QPT mediated by the Griffith phase is also reflected in $M(H)$ curves, which follow anomalous power laws $M \sim H^{\alpha}$ and $M - M_0 \sim H^{\alpha}$ in the paramagnetic and ferromagnetic regions, respectively [2,34,35]. Here M_0 is the spontaneous magnetization and α is a nonuniversal exponent, strongly dependent on x and decreasing towards zero at x_c. Figure 11(a) shows the fitting of the experimental magnetization curves of $Co_{1+x}Sn$ ($0.45 \leqslant x \leqslant 0.65$) for a field region 7 to 70 kOe using $M \sim H^{\alpha}$, with α obtained using the fitting as shown as a function of x in Fig. 11(b). Note that α is also reported to follow a power law $\alpha(x) \sim (x_c - x)^{\zeta}$ ($\zeta = \nu\psi$ in [Ref. [2]], where ν is different from the exponent ν discussed in Sec. I), and we have fitted α values of the paramagnetic $Co_{1+x}Sn$ samples using the above equation and $x_c = 0.65$ determined from Fig. 10. This analysis also yields $\zeta = 0.47$, which strikingly is the same as β'. On the ferromagnetic side, α is strongly affected by a number of factors, such as the size distribution of the nonpercolated (unconnected) clusters, random anisotropy, and domain formation. Therefore, we have not attempted to explicitly analyze this aspect of the QPT for the ferromagnetic samples. Note that $\alpha(x)$ is reported in [Ref. [2]] to be nearly symmetric on both sides of x_c, and thus a symmetric $\alpha(x)$ curve for the ferromagnetic side is also drawn as a dashed line in Fig. 11(b) to visualize clearly the critical behavior near the quantum critical point. However, the abrupt magnetization jump near x_c shown in Fig. 10 is consistent with the finding in [Ref. [2]] that α goes to zero as x approaches x_c.

It is also important to distinguish QPTs involving strong and weak itinerant ferromagnets. In strong ferromagnets, the majority ($\uparrow$) band is completely filled, so that any change in x simply reduces or enhances the number of $3d$ electrons in the minority ($\downarrow$) band. As a consequence, the saturation magnetization changes linearly with x, and the exponent in $M_s \sim (x - x_c)^{\beta'}$ is $\beta' = 1$. A very similar scenario is realized when the Fermi level is captured in the vicinity of some peak. Examples of this strong ferromagnetism are $Ni_{1-x}V_x$ and $Ni_{1-x}Cu_x$ [34,52]. In weak ferromagnets, such as bcc Fe, the $\uparrow$ and $\downarrow$ $3d$ bands are partially but not equally filled, so $M \sim n_{\uparrow} - n_{\downarrow}$ is nonzero. Since changes in x affect both subbands, they make the difference $n_{\uparrow} - n_{\downarrow}$ very small in some alloys without complete band filling, which is known as very weak itinerant ferromagnetism (VWIF). This scenario is realized in materials such as $ZrZn_2$ [30,53,54] and $Co_{1+x}Sn$ as discussed below.

The simplest quantum-mechanical approach is to evaluate the magnetic energy in terms of Eqs. (4) and (5). The interesting physics is in the parameter $a_2 \sim 1/\mathcal{D}(E_F) - I$. The parameter a_4 exhibits a more complicated dependence on $\mathcal{D}(E_F)$ [30], but it is generally on the order of $1\,\text{eV}/\mu_B{}^4$ if M is measured in μ_B per atom. The magnetization is obtained

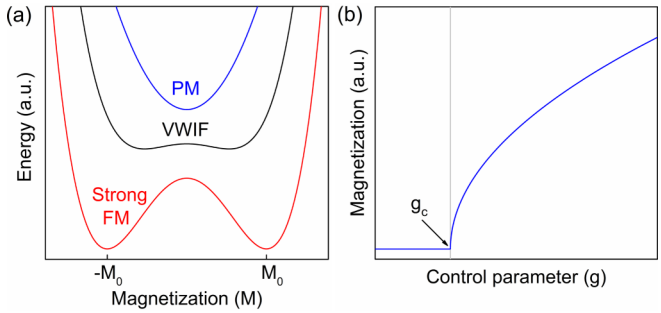

FIG. 12. Predictions from Eq. (4): (a) magnetic energy as a function of magnetization for paramagnet, very weak itinerant ferromagnet, and strong ferromagnet and (b) magnetization as a function of the control parameter $g \sim \mathcal{D}(E_F) \sim x$.

by finding the minima of E, that is, by putting $\partial E/\partial M = 0$ in Eq. (4). For $H = 0$, this yields the spontaneous magnetization, whereas the application of a small field yields the susceptibility, $\chi = \mu_0/a_2$ in the case of exchange-enhanced Pauli paramagnetism [Eq. (5)]. Figure 12(a) shows $E(M)$ for different regimes. In the paramagnetic state (blue curve), a_2 is positive and large, which yields a deep magnetic-energy minimum at $M = 0$ and a very small Pauli susceptibility. In strong ferromagnets, a_2 is large but negative, so that the magnetic energy exhibits two deep minima (red curve). This corresponds to spontaneous symmetry breaking and to a ferromagnetic ground state with $|M| = M_0$, where M_0 roughly corresponds to full spin polarization, about $2\mu_B$ per atom for metallic Co. With decreasing a_2, physically realized through $\mathcal{D}(E_F)$, the susceptibility increases and reaches infinity at the Stoner transition ($a_2 = 0$). Note that Fig. 12(a) is very similar to the Landau theory of finite-temperature phase transitions [55].

Figure 12(a) also shows the energy landscape for the very weak itinerant ferromagnetic case, where the Stoner criterion is barely satisfied (black curve). In this case, the spontaneous magnetization $M_{\min}$ is substantially smaller than M_0. Figure 12(b) shows how $M_{\min}$ varies as a function of the control parameter $g = -a_2$. The density of states is a function of x, so that g can approximately be linearized near g_c; thus, x rather than g can be used on the horizontal axis of Fig. 12(b). In more detail, putting $\partial E/\partial M = 0$ and $H = 0$ in Eq. (4) yields a square-root dependence $M \sim (-a_2)^{1/2}$, which is schematically shown in Fig. 12(b). Writing $\mathcal{D}(E_F) = \mathcal{D}_s + b(x - x_c)$, where $\mathcal{D}_s$ corresponds to the Stoner transition, putting the linearized expression into a_2, and analyzing M as a function of x yields $M \sim (x - x_c)^{1/2}$, that is, $\beta' = 1/2$.

The existence or nonexistence of a quantum phase transition having $\beta' = 1/2$ depends on the electronic structure of the material. Equation (4) is an analytic function of E on M, but densities of states and the resulting magnetic energies are generally nonanalytic. The nonanalyticity is most pronounced in strong ferromagnets, where the two minima stay far apart at $\pm M_0$ even very close to the Stoner transition [56]. As discussed above, our experiments as well as density-functional calculations support an exponent $\beta' = 1/2$ rather than $\beta' = 1$ in $Co_{1+x}Sn$.

The minima in the black curve of Fig. 12(a) are very shallow, the energy difference scaling as ${a_2}^2$, which means that perturbations have a very strong impact on the system's behavior. Three types of perturbations need to be considered. First, quantum fluctuations reflect Heisenberg's uncertainty principle [57,58]. In strongly exchange-enhanced Pauli paramagnets, which are close to the Stoner transition and characterized by small but positive values of a_2, quantum fluctuations have the character of temporarily stable paramagnons [57]. These quasiparticles affect, for example, the specific heat [29]. Second, at $T > 0$, the effect of the quantum fluctuations is enhanced by thermal fluctuations, which is known as the quantum critical region. Third, chemical disorder acts as a strong perturbation and profoundly alters the physical behavior of the system. In the present systems, the disorder is of the interstitial type.

In terms of Eq. (5), quantum effects due to interstitial disorder correspond to the k dependence of the susceptibility, whereas in density-functional theory they are described in terms of supercells (Fig. 8). One aspect of the system is the existence of Griffiths phenomena in the paramagnetic phase, caused by regions rich in interstitial Co. By itself, the Griffiths phase [33] is a classical phenomenon, because it deals with the Ising model [28], where all operators commute. Note that this proper or statistical Ising model differs from the so-called transverse Ising model [57,59], both models being important in the theory of phase transitions. However, the quantum-mechanical interactions leading to the formation of Griffiths clusters in the present case are quite different from the random-Ising and substitutional-alloy systems considered so far.

In the analysis of the QPT, we take into account that the Co-Sn alloys are only weakly correlated, so that density-functional theory and Eq. (5) can be used to determine the spin state. If the magnetism of the Co atoms were of the strong type, then each Co atom would have a stable magnetic moment, and the total moment would be proportional to the number of Co atoms. This is not the case here: Hypothetical CoSn is (almost certainly) Pauli-paramagnetic, and the situation does not change very much for small amounts of excess cobalt. In particular, the DFT calculations and our experiments show that single Co atoms on interstitial sites do not develop a Co moment. However, once the interstitial Co atoms cluster, they develop a moment and also spin polarize the surrounding host-lattice Co atoms. This scenario is described by Fig. 8 and very different from strong ferromagnetism, where the Co moment is determined by band-filling effects but otherwise stable. Spatial moment fluctuations are described through the k dependence in Eq. (5). The onset of ferromagnetism in $Co_{1+x}Sn$ involves fairly large numbers of Co atoms, about 17 in Fig. 8(b), but these regions are not infinite. Their finite size corresponds to nonzero k values in Eq. (5) and therefore works against the Stoner parameter I, which is the driving force behind the onset of ferromagnetism.

Once the Co clusters grow with increasing x, the Co atoms inside the clusters rapidly develop fairly stable moments (Sec. II B). This situation is reminiscent of strong ferromagnetism but difficult to distinguish experimentally from the VWIF scenario, because both Fig. 12(b) and the number of Co atoms in the percolation backbone yield similar exponents $\beta' \approx 0.5$ above x_c.

IV. CONCLUSIONS

In summary, we have shown a quantum phase transition in $Co_{1+x}Sn$, caused by excess Co (x) occupying interstitial sites. Below the critical composition $x_c = 0.65$, the material is paramagnetic, combining Griffiths-phase and Pauli-paramagnetic features, whereas at above x_c, the excess Co triggers a transition to ferromagnetism. Isolated interstitial Co atoms do not develop a local magnetic moment, in spite of being embedded in a Co-rich matrix, but clusters of interstitial Co atoms do and also spin polarize the surrounding host lattice. The transition involves two types of exchange interactions, namely a relatively strong Co-Co exchange mediated by host-lattice Co atoms and a much weaker exchange between Co-rich clusters.

We hope that our analysis of the onset of ferromagnetism in Co-Sn deepens the understanding of quantum phase transitions in itinerant-electron systems, drawing attention to both universal and nonuniversal features.

ACKNOWLEDGMENTS

This research is primarily supported by the US Department of Energy (DOE) under Awards No. DE-FG02-04ER46152 and No. DE-FG02-90ER45413 at Nebraska and Delaware, respectively. Research at Nebraska was performed in part in the Nebraska Nanoscale Facility: National Nanotechnology Coordinated Infrastructure and the Nebraska Center for Materials and Nanoscience, which are supported by the National Science Foundation under Award No. NNCI-1542182, and the Nebraska Research Initiative. We would also like to acknowledge the support at Ames Laboratory and Nebraska by National Science Foundation under Awards No. DMREF 1729677 and No. DMREF:SusChEM 1729288, respectively, for the discovery of magnetic materials. Ames Laboratory is operated for the US DOE by Iowa State University under Contract No. DE-AC02-07CH11358.

[1] M. Brando, D. Belitz, F. M. Grosche, and T. R. Kirkpatrick, Rev. Mod. Phys. **88**, 025006 (2016).
[2] R. Wang, A. Gebretsadik, S. Ubaid-Kassis, A. Schroeder, T. Vojta, P. J. Baker, F. L. Pratt, S. J. Blundell, T. Lancaster, I. Franke, J. S. Möller, and K. Page, Phys. Rev. Lett. **118**, 267202 (2017).
[3] T. R. Kirkpatrick and D. Belitz, Phys. Rev. B **91**, 214407 (2015).
[4] T. Vojta, Ann. Phys. **9**, 403 (2000).
[5] T. Vojta, Annu. Rev. Condens. Matter Phys. **10**, 233 (2019).
[6] H. v. Löhneysen, A. Rosch, M. Vojta, and P. Wölfle, Rev. Mod. Phys. **79**, 1015 (2007).
[7] S. Sachdev, Nat. Phys. **4**, 173 (2008).
[8] P. C. Canfield, Nat. Phys. **4**, 167 (2008).
[9] R. Skomski, AIP Adv. **6**, 055704 (2016).
[10] D. M. Broun, Nat. Phys. **4**, 170 (2008).
[11] N. D. Mathur, F. M. Grosche, S. R. Julian, I. R. Walker, D. M. Freye, R. K. W. Haselwimmer, and G. G. Lonzarich, Nature (London) **394**, 39 (1998).
[12] P. Gegenwart, Q. Si, and F. Steglich, Nat. Phys. **4**, 186 (2008).
[13] P. Chandra, G. G. Lonzarich, S. E. Rowley, and J. F. Scott, Rep. Prog. Phys. **80**, 112502 (2017).
[14] M. Uhlarz, C. Pfleiderer, and S. M. Hayden, Phys. Rev. Lett. **93**, 256404 (2004).
[15] J. Paglione, M. A. Tanatar, D. G. Hawthorn, E. Boaknin, R. W. Hill, F. Ronning, M. Sutherland, L. Taillefer, C. Petrovic, and P. C. Canfield, Phys. Rev. Lett. **91**, 246405 (2003).
[16] L. Demkó, S. Bordács, T. Vojta, D. Nozadze, F. Hrahsheh, C. Svoboda, B. Dóra, H. Yamada, M. Kawasaki, Y. Tokura, and I. Kézsmárki, Phys. Rev. Lett. **108**, 185701 (2012).
[17] P. Swain, S. K. Srivastava, and S. K. Srivastava, Phys. Rev. B **91**, 045401 (2015).
[18] L. Schoop, M. Hirschberger, J. Tao, C. Felser, N. P. Ong, and R. J. Cava, Phys. Rev. B **89**, 224417 (2014).
[19] M. Ellner, J. Less-Common Met. **48**, 21 (1976).
[20] H. Fjellvag and A. Kjekshus, Acta Chem. Scand., Ser. A **40**, 23 (1986).
[21] X. Zhao, M. C. Nguyen, W. Y. Zhang, C. Z. Wang, M. J. Kramer, D. J. Sellmyer, X. Z. Li, F. Zhang, L. Q. Ke, V. P. Antropov, and K.-M. Ho, Phys. Rev. Lett. **112**, 045502 (2014).
[22] B. Balasubramanian, B. Das, M. C. Nguyen. X. Xu, J. Zhang, X. Zhang, Y. Liu, A. Huq, S. R. Vallopilly, Y. Jin, K.-M. Ho, C.-Z. Wang, and D. J. Sellmyer, APL Mater. **4**, 116409 (2016).
[23] B. Balasubramanian, X. Zhao, S. R. Vallopilly, S. Beniwal, R. Skomski, A. Sarella, Y. Jin, X. Z. Li, X. Xu, H. Cao, H. Wang, A. Enders, C.-Z. Wang, K.-M. Ho, and D. J. Sellmyer, Nanoscale **10**, 13011 (2018).
[24] J. M. Yeomans, *Statistical Mechanics of Phase Transitions* (Clarendon, Oxford, 1992).
[25] K. G. Wilson, Rev. Mod. Phys. **55**, 583 (1983).
[26] J. Shen, R. Skomski, M. Klaua, H. Jenniches, S. S. Manoharan, and J. Kirschner, Phys. Rev. B **56**, 2340 (1997).
[27] R. Skomski, *Simple Models of Magnetism* (Oxford University Press, Oxford, 2008).
[28] E. Ising, Z. Phys. **31**, 253 (1925).
[29] W. Jones and N. H. March, *Theoretical Solid State Physics I* (Wiley & Sons, London, 1973).
[30] P. Mohn, *Magnetism in the Solid State* (Springer, Berlin, 2003).
[31] K. K. Murata and S. Doniach, Phys. Rev. Lett. **29**, 285 (1972).
[32] P. Fulde, *Electron Correlations in Molecules and Solids* (Springer, Berlin, 1991).
[33] R. B. Griffiths, Phys. Rev. Lett. **23**, 17 (1969).
[34] S. Ubaid-Kassis, T. Vojta, and A. Schroeder, Phys. Rev. Lett. **104**, 066402 (2010).
[35] T. Westerkamp, M. Deppe, R. Küchler, M. Brando, C. Geibel, P. Gegenwart, A. P. Pikul, and F. Steglich, Phys. Rev. Lett. **102**, 206404 (2009).
[36] M. J. Case and V. Dobrosavljević, Phys. Rev. Lett. **99**, 147204 (2007).
[37] J. W. Essam, Rep. Prog. Phys. **43**, 833 (1980).
[38] D. Stauffer and A. Aharony, *Introduction to Percolation Theory* (Taylor & Francis, London, 1992).
[39] International Centre for Diffraction Data, Powder Diffraction File Card No. 00-027-1124.
[40] G. C. Hadjipanayis, D. J. Sellmyer, and B. Brandt, Phys. Rev. B **23**, 3349 (1981).

[41] P. W. Anderson, Phys. Rev. **124**, 41 (1961).
[42] G. Kresse and D. Joubert, Phys. Rev. B **59**, 1758 (1999).
[43] J. P. Perdew, K. Burke, and M. Ernzerhof, Phys. Rev. Lett. **77**, 3865 (1996).
[44] H. J. Monkhorst and J. D. Pack, Phys. Rev. B **13**, 5188 (1976).
[45] R. J. Elliott, J. A. Krumhansl, and P. L. Leath, Rev. Mod. Phys. **46**, 465 (1974).
[46] H. Ebert *et al.*, The Munich SPR-KKR package, Version 7.7 (2017).
[47] H. Ebert, D. Ködderitzsch, and J. Minár, Rep. Prog. Phys. **74**, 096501 (2011).
[48] M. Goano, E. Bellotti, E. Ghillino, C. Garetto, G. Ghione, and K. F. Brennan, J. Appl. Phys. **88**, 6476 (2000).
[49] E. N. Economou, *Green's Functions in Quantum Physics* (Springer, Berlin, 1979).
[50] R. Skomski, J. Appl. Phys. **101**, 09N517 (2007).
[51] D. S. Fisher, Phys. Rev. Lett. **69**, 534 (1992).
[52] S. Chikazumi, *Physics of Magnetism* (Wiley, New York, 1964).
[53] E. P. Wohlfarth, J. Appl. Phys. **39**, 1061 (1968).
[54] P. Mohn and E. P. Wohlfarth, J. Phys. F: Met. Phys. **17**, 2421 (1987).
[55] R. Skomski, B. Balamurugan, P. Manchanda, M. Chipara, and D. J. Sellmyer, IEEE Trans. Magn. **53**, 2300307 (2017).
[56] R. Skomski and J. M. D. Coey, *Permanent Magnetism* (Institute of Physics, Bristol, 1999).
[57] J. A. Hertz, Phys. Rev. B **14**, 1165 (1976).
[58] S. Sachdev, Phys. World, **12**, 33 (1999).
[59] R. B. Stinchcombe, J. Phys. C **6**, 2459 (1973).